Fuel 265 (2020) 116979

Contents lists available at ScienceDirect

Fuel

journal homepage: www.elsevier.com/locate/fuel

Full Length Article

An evaluation of kerogen molecular structures during artificial maturation

Tian Liang[a,b], Yan-Rong Zou[a,*], Zhao-Wen Zhan[a], Xiao-Hui Lin[a,b], Jun Shi[a,b], Ping'an Peng[a,b]

[a] Guangzhou Institute of Geochemistry, China Academy of Sciences, Guangzhou 510640, China
[b] University of Chinese Academy of Sciences, Beijing 100049, China

ARTICLE INFO

Keywords:
Kerogen
Molecular Structure
^{13}C NMR
XPS
Condensation

ABSTRACT

^{13}C solid-state NMR and XPS techniques were used to investigate structural changes in kerogen during oil generation process across a range of maturity. Kerogen was isolated from an shale rock collected from Well W161 in the Dongying Depression, Bohai, China. An artificial pyrolysis experiment was carried out in a closed gold tube system using a heating rate of 2 °C/h during which 11 temperature-point samples were collected between 350 °C and 450 °C (Easy%Ro = 0.80 to 1.98). The initial kerogen was analysed using Rock-Eval and the samples were analysed using X-ray photoelectron spectroscopy (XPS) and solid-state ^{13}C nuclear magnetic resonance (^{13}C NMR) to study their functional groups and chemical structures. Six averaged molecular structure models of the initial kerogen and its residues (can not be dissolved by organic reagent) were established to study the changes occurring during oil and gas generation. The results showed that with an increase in temperature, the proportion of aliphatic carbon declined while aromatic carbon increased. After reaching peak oil maturity, a condensation reaction occurred in the residue; some aromatic carbons cracked from the kerogen and combined with the residue structure. Average aromatic cluster increment was calculated to quantify the increase in the size of aromatic clusters within the structures. It was established to evaluate the changes occurring in the molecular structure of type I kerogen during heating. Based on these results, Con_U (maximum condensation degree) and Con_L (lowest condensation degree) are proposed to estimate the degree of condensation of samples with different maturities.

1. Introduction

Rising global energy demand continues to increase the need for fossil energy sources, and oil shale rocks—which can supply conventional oil and gas—is gaining attention [1]. Oil shale rocks consist of both organic matter and inorganic minerals. Since kerogen is an important part of naturally occurring organic matter [2,3] and is the source of oil from oil shale rocks [4], the yield of shale oil depends on the quality and quantity of kerogen. Moreover, the molecular structure of kerogen plays a key role in shale oil yields [5]. To study the changes in the structure of kerogen occurring during its evolution, CP-TOSS/MAS solid-state ^{13}C nuclear magnetic resonance (NMR) has been used to assess the molecular characteristics of different kerogen types [6–8]. Since Burlingame (1969) [9] established the molecular structure of Green River Shale (GRS), more and more research on the structure of kerogen has been undertaken. Recently, three-dimensional (3D) molecular structure modelling techniques have been established for kerogen and other fossil organic matter [10–12]. The majority of previous studies on kerogen have focused on its general characteristics or its initial structure. Some studies have concentrated on specific features of the molecular structure of kerogen during oil generation, such as aliphatic carbon, heteroatoms and minerals [13,14]. However, there are few studies of corresponding molecular models in the heating evolution process [15–17].

Molecular simulation has provided a detailed picture of the structure of kerogen [18]. Hence, it is important to study its molecular structure to better understand the molecular-level changes occurring during oil and gas generation. Understanding these changes could provide important insights into the mechanisms of petroleum formation [19]. As it is difficult to obtain kerogen of continuous maturity states in nature, artificially matured kerogen is widely used to study gas, oil and kerogen during pyrolysis [20–22]. For this, kerogen samples are heated artificially and molecular models are established to study the evolutional regulation of oil generation.

^{13}C NMR has been widely applied in the study of the structure of kerogen and other fossil organic samples [23–26]. This technique can provide information on how carbon atoms are connected by distinguishing the chemical shifts of different kinds of carbon atoms [27,28]. Since carbon atoms are a major element of the structure of kerogen, ^{13}C NMR offers fundamental data for establishing molecular models. In

* Corresponding author.
E-mail address: zouyr@gig.ac.cn (Y.-R. Zou).

https://doi.org/10.1016/j.fuel.2019.116979
Received 31 May 2019; Received in revised form 4 December 2019; Accepted 29 December 2019
Available online 07 January 2020
0016-2361/

addition to ^{13}C NMR, ^{29}Si NMR has also been used to research the selective chemical derivatisation of kerogen [29]. X-ray photoelectron spectrometry (XPS) is another useful technique for providing quantitative and qualitative details of the connections between not only organic carbon atoms but also organic heteroatom functional groups (i.e. organic oxygen, organic nitrogen and organic sulphur) in complex compounds [30–33].

In this study, kerogen was isolated from the Dongying type I source rock and subjected to a hydrocarbon generation experiment under anhydrous pyrolysis. Then, the initial kerogen and residues are analysed by ^{13}C NMR and XPS to determine their molecular structures. Using this information, six general molecular models are established to represent the characteristics of the initial kerogen and its residues during oil and gas generation. Furthermore, the chemical shifts of molecular models are calculated and compared with the results of the ^{13}C NMR. The models are subsequently modified to obtain the required level of accuracy. In doing so, basic molecular models are provided of different maturities that should prove useful for further research including the study of 3D structure and gas adsorption [34,35].

2. Materials and methods

The rock core used in the experiments was obtained from Well W161 of the Dongying Depression, Bohai Bay Basin, eastern China, at a depth of 1,911.9 m. The lithology of the core was shale (Type I lacustrian source rock). The rock core was ground into powder (< 200 mesh size, approximately 0.075 mm) and mixed with reagents (dichloromethane and methanol, at a volume ratio of 93:7) for 72 h to extract soluble organic matter. Hydrochloric acid (6 mol/L) and hydrofluoric acid (6–8 mol/L) were used to remove carbonates and destroy Si-O bonds (mainly silicates and quartz) in the rock. After the acid treatment, the acid in the sample and the soluble organic matter absorbed by the minerals were removed by washing with distilled water and by extracting with dichloromethane and methanol (93:7), respectively. As a result of these treatments, the pure kerogen samples were obtained [17,36,37].

Rock-Eval VI plus was used to evaluate the kerogen samples. Approximately 5 mg of kerogen powder was used for this analysis in each case. The kerogen samples were heated to 300 °C in 3 min under nitrogenous conditions. Then, the temperature was increased to 600 °C using a heating rate of 25 °C/min. The thermal maturity and hydrocarbon generation potential of the kerogen samples were then estimated as presented in Table 1.

Anhydrous pyrolysis was used to prepare a series of kerogen samples of differing maturities. Easy%Ro [38], a simple model to evaluate the vitrinite reflectance of kerogen, was then used to evaluate the maturity of the samples. The initial kerogen was placed into gold tubes, which were welded at one end, and the air in each of the tubes was replaced with argon to exclude the influence of oxygen. The tubes were then welded under an argon atmosphere and placed into stainless-steel vessels. This meant that every vessel represented a defined temperature point in this experiment. After this preparation, the vessels were placed into a furnace at 50 MPa pressure and heated to 300 °C over 8 h, and these conditions were maintained for 2 h. Next, the temperature of the furnace was increased to 450 °C at a rate of 2 °C/h. During the heating process, the tubes were removed every ten degrees (between 350 °C and 450 °C) giving 11 sampling points. The products of this treatment were then extracted using a dichloromethane and methanol mixture (93:7) for 72 h to obtain solid residues [17,39]. Finally, the residues were analysed using ^{13}C NMR and XPS.

A K-Alpha X-ray photoelectron spectrometer (Thermo Fisher Scientific, UK) with a monochromatic AI Kα X-ray source (1,468.6 eV) was employed in this study. At the beginning of the analysis, a vacuum was created inside the analysis chamber ($< 5 \times 10^{-8}$ mbar). Analysis spectra were maintained at 0 to 1,350 eV using an X-ray spot size of 400 μm with pass energy of 100 eV for wide-scanning and 30 eV for individual elements [40]. XPS analysis was used to detect organic functional groups.

All ^{13}C NMR analyses was conducted using a Bruker AVANCE III at 400 MHz 1H and 100 MHz 13C frequencies with a 4-mm double-resonance probe head and a ZrO_2 rotor. The spinning speed was 5,000 Hz and the CP-TOSS/MAS (TOSS: total side band suppression; MAS: magic angle spinning CP: Cross polarization) method was used to test the sample structures and suppress the side-bands. The spectral width was 100,000 Hz. The recycle delay time was 1 s and the number of scans was 4,000. Considering the ^{13}C CP/TOSS NMR technique has its inherent deficiency in the estimation of non-protonated aromatic carbons. In this research, the purpose of solid-state NMR test was to study the changes of kerogen structure in the process of oil production rather than quantitative study of functional groups [15].

3. Results and discussion

3.1. Basic geochemical parameters

The basic geochemical parameters of the initial kerogen samples are shown in Table 1, where S_2 (the amount of hydrocarbons generated through thermal cracking of nonvolatile organic matter) was 287 HC mg/g, the HI (hydrogen index, HI = (100 × S2)/TOC) was 714 HC mg/g TOC, and the T_{max} (the temperature at which the maximum release of hydrocarbons from cracking of kerogen occurs during pyrolysis) was 436 °C. According to Eq. (1) [41], the calculated Ro% (vitrinite reflectance) was 0.68.

$$Ro\% = 0.018 \times T_{max} - 7.16 \quad (1)$$

Table 1 indicates that this was a type I, oil-prone kerogen.

3.2. Pyrolysis products

The pyrolysis products were separated into soluble matter and residues (can not be dissolved by organic reagent), which were collected from the reagent and the Soxhlet extractors, respectively. A total of 11 temperature point residues were ground and weighted for subsequent analysis.

Fig. 1 presents the residue weight ratios (i.e. residue weight:initial weight), which shows that the weight ratio of residues decreased from 0.56 to 0.32 when the temperature was increased from 360 °C to 390 °C (Easy%Ro increased from 0.86 to 1.15) around the maturity of oil peak. Above 390 °C, the ratio gradually increased to 0.63 (440 °C). The initial kerogen cracked within the first temperature range (from 360 °C to 390 °C) when small molecular structures separated from the kerogen and were converted to oil and gas. This reaction resulted in the reduction of the residue ratio. After the maturity of oil peak, a condensation reaction occurred in the kerogen under the high temperatures [42,43] indicating that the size of average kerogen (residue) molecular structures initially decreased (below 390 °C) and stabilised after the oil peak.

Table 1
Geochemical parameters of the initial kerogen.

Sample	Type	TOC %	T_{max} °C	S_1 mg HC/g	S_2 mg HC/g	PI	HI mg HC/g TOC	PC %	D %
W161	I	40.22	436	12.08	287	0.04	714	24.82	61.72

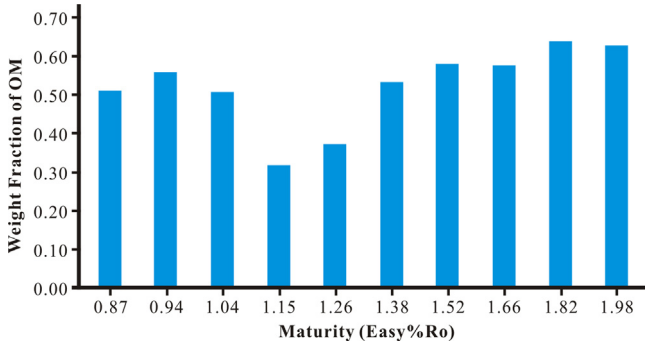

Fig. 1. Relative residue weight ratios.

3.3. XPS analysis

XPS was used to detect the relative proportions of C, N, O and S to qualitatively describe the functional groups of these elements [44].

3.3.1. Changes in relative element content

Carbon was predominant, at more than 80%, in the residual kerogen (Fig. 2a), showing a sudden decrease near the oil peak maturity. The relative content of carbon decreased from 87.78% to 81.95% (Easy%Ro increased from 0.68 to 1.15) and then increased to 87.04%, which was similar to the variation of the weight ratio of the residue (Fig. 1), as caused by cracking and condensation. Oxygen was the second most abundant component in the residues (10–14%, Fig. 2b), although the changes in the percentage of oxygen were opposite to carbon. The relative content of oxygen increased from 9.80% to 14.32% (Easy% Ro = 0.68 to 1.15) followed by a decline to 11.03% during the remaining heating time. It can be inferred that the average energy of the residual oxygen atom pairs was larger than the average energy of the carbon atom pairs. This would lead to a relatively more stable connection between oxygen atoms in the Ro range of 0.68–1.15, while the aliphatic chain will be broken within the same Ro range. In the Ro range of 1.26–1.98, the kerogen was enlarged due to pairing reactions, leading to an increase in the relative carbon content [43]. However, oxygen either showed no apparent change or limited cracking in this range. These differences between carbon and oxygen affected the observed changes in the relative oxygen content.

The relative proportions of nitrogen and sulphur elements were small (Fig. 2c and 2d, respectively). The proportion of nitrogen was less than 2.17% during the entire heating process and there was no apparent change in its relative proportion. This could result from the absolute content of nitrogen in the kerogen being very low and mostly present in the form of pyrrole and pyridine, which are difficult to break under these experimental temperatures. Therefore, the relative nitrogen content varied from 0.78% to 2.17%. Similarly, the relative proportion of sulphur was low and varied from 0.35% to 1.81%. Both nitrogen and sulphur occurred at low proportions in the kerogen, and the oxygen ratio was significantly affected by the carbon content. Hence, this study focused on the nature of the bonds between the carbon atoms.

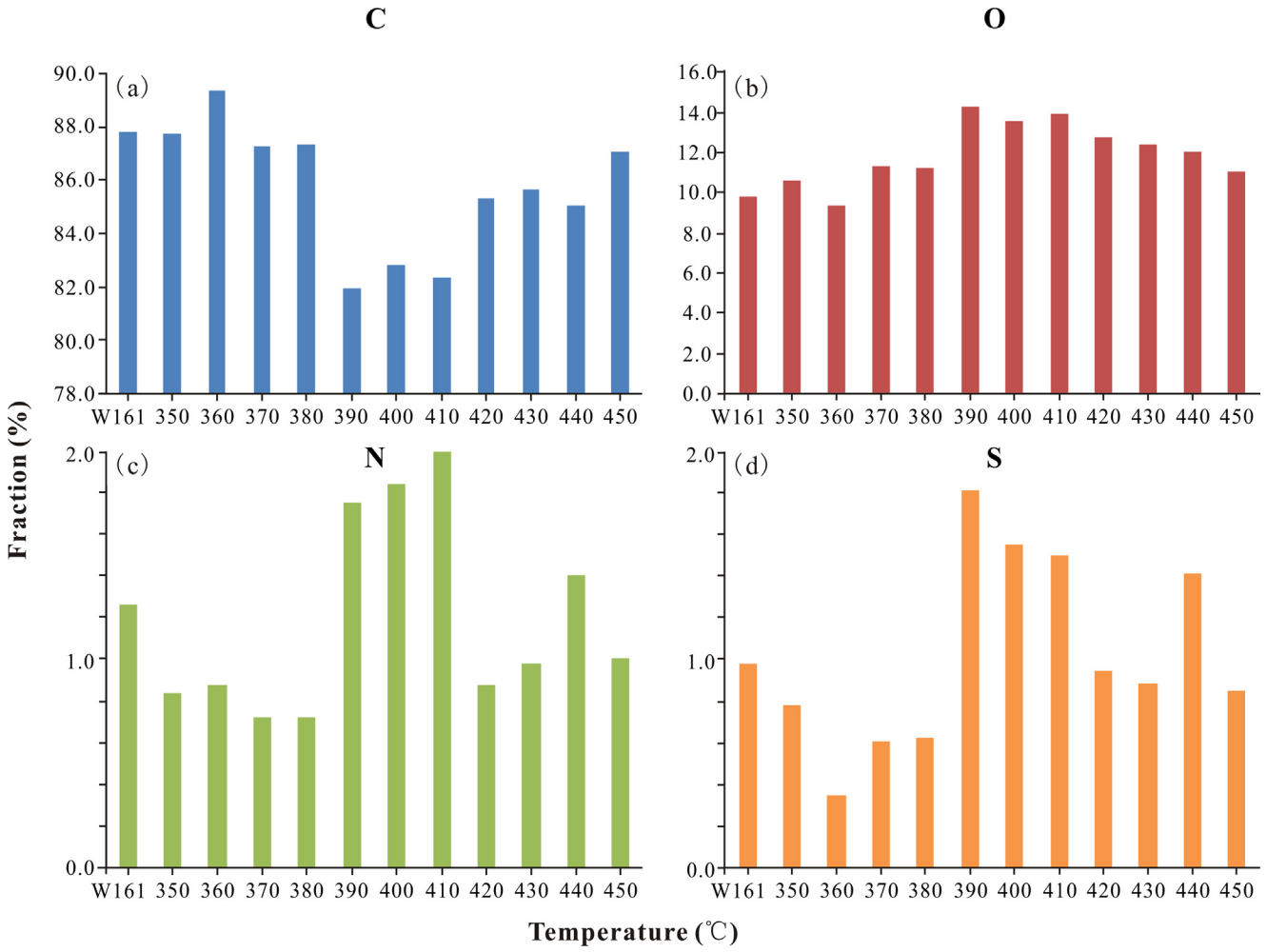

Fig. 2. Elemental content of the kerogen and residue samples.

Table 2
Elements and functional group contents.

Sample	C %						N %			O %		S %		
	C−C	C−O	O−C−O	C═O	O−C═O	O−C−C	Amine	Pyrrolic	Pyridinic	O−C	O═C	Aliphatic	Sulfoxide	Thiophenic
W161	82.86	3.64	1.43	1.74	0.00	0.00	0.59	0.00	0.00	6.15	3.26	0.13	0.07	0.13
350°C	79.57	7.04	0.99	0.00	4.94	0.00	0.00	0.00	0.10	5.45	1.70	0.09	0.11	0.00
360°C	85.63	5.80	0.79	0.00	0.00	1.72	0.16	0.00	0.00	4.28	1.55	0.00	0.01	0.07
370°C	82.23	3.34	1.43	0.68	0.00	1.66	0.00	0.00	0.12	8.88	1.43	0.09	0.06	0.09
380°C	80.11	5.89	1.49	0.00	0.00	0.00	0.00	0.12	0.19	9.06	2.88	0.09	0.07	0.09
390°C	77.90	5.17	1.35	1.78	0.00	0.70	0.00	1.33	0.00	8.12	2.96	0.35	0.35	0.00
400°C	78.19	3.83	0.00	1.37	3.38	0.00	0.00	0.58	0.53	5.66	5.59	0.44	0.00	0.44
400°C	78.77	5.62	0.00	1.80	0.00	1.98	0.00	0.57	0.53	6.42	3.70	0.12	0.07	0.41
410°C	83.24	1.49	1.42	0.00	0.00	1.60	0.00	0.32	0.16	7.86	3.31	0.30	0.00	0.30
420°C	72.65	11.27	2.15	1.46	0.00	0.29	0.00	0.43	0.00	7.82	3.30	0.29	0.05	0.29
430°C	81.14	2.47	2.03	2.01	0.00	0.69	0.56	0.00	0.00	5.95	4.24	0.45	0.45	0.00
450°C	84.87	1.75	1.34	0.24	0.00	0.00	0.17	0.33	0.00	5.90	4.73	0.33	0.33	0.00

3.3.2. Functional group changes

The relative proportions of the organic functional groups (C, N, O and S) are listed in Table 2. In the carbon spectrum, there were four peaks, at 284.5, 286.2, 287.4 and 289.0 eV, representing C−C (aliphatic and aromatic carbon), C−O, C═O (carbonyl), and O−C−O or O═C−O (carboxyl), respectively [45,46]. C−C was the largest functional group in both the initial kerogen and residues, with a relative proportion above 70%. C−O was the second-largest functional group, with the relative proportion of 3–10%. Both C−C and C−O formed the basic molecular skeleton of the kerogen. The content of O−C−O and C═O was significantly lower than C−C and C−O. The ratio of O−C−O and C═O varied between 0% and 2.5%. There were few O−C═O and O−C−C functional groups in the sample structures, and these two functional groups did not occur in half of the samples.

Organic nitrogen had three major peaks, at 398.8, 399.5 and 400.2 eV, which represented pyridinic, amine and pyrrolic, respectively. Pyridinic and pyrrolic were the main forms of organic nitrogen. During the high-temperature stage (from 400 °C to 450 °C), the relative proportion of pyrrolic remained more stable than pyridinic (Table 2).

The oxygen-containing functional groups were O−C and O═C, and their peaks were found near 531.4 eV and 532.8 eV, respectively. The proportion of O−C was larger than that of O═C in the samples. This means that O−C was the dominant connection between the oxygen atoms. The proportions of both O−C and O═C did not decrease with an increase in temperature (Table 2), indicating that the oxygen atoms did not easily separate from the residual kerogen structure.

There were three kinds of organic sulphur functional groups: (1) aliphatic sulphur, (2) thiophenic and (3) sulfoxide, with peaks at 162.8, 164.3 and 166.0 eV, respectively. The proportion of sulphur atoms was small, and the main form of sulphur atoms was aliphatic sulphur. The proportions of thiophenic and sulfoxide were approximately 0.5%, and some samples lacked these functional groups completely. The number of sulphur atoms per 100 atoms (C, N, O and S) was also less than one, and this did not decrease as the temperature increased.

3.4. Solid-State ^{13}C NMR

3.4.1. General ^{13}C NMR characteristics

Solid-state ^{13}C NMR is useful in characterising the structure of organic matter [47]. Aliphatic carbon and aromatic carbon are two important components of the structure of kerogen, with chemical shifts at 5–95 ppm and 95–150 ppm, respectively [48]. The ^{13}C NMR spectra are presented in Fig. 3, with maturity increasing from 350 °C to 450 °C. During the experiment, the proportion of aliphatic carbon decreased, while the proportion of aromatic carbon increased (Fig. 3). This could have been caused by different binding energies between the aromatic and aliphatic carbon. Several aliphatic chains and a few small-sized aromatic groups broke away from the kerogen during the oil and gas generation process, while the large-sized aromatic clusters remained. At the oil peak (Easy%Ro = 0.86), the aromatic carbon exceeded the aliphatic chains (Fig. 3), which has also been observed previously [39]. With the occurrence of condensation at high temperatures, aromatic groups that had broken from the kerogen would have combined with the residues and became a part of their structures. These two reactions explain the observed changes in the proportions of aliphatic carbon and aromatic carbon.

The NMR spectral peaks were assigned and integrated to determine the relative content of each functional group. All of the functional group proportions are listed in Table 3.

3.4.2. Aliphatic carbon

The aliphatic carbon proportion decreased from 63.43% to 4.33% during the maturation process (Table 3). There were six kinds of aliphatics: (1) aliphatic methyl (f_{al}^{CH3}), (2)aromatic methyl (f_{ar}^{CH3}), (3) methylene (f^{CH2}), (4) methine (f^{CH}), (5) quaternary (f^{C}) and (6) O-alkyl (f^{O}), with chemical shifts occurring at 10–19 ppm, 19–22 ppm, 22–35 ppm, 35–40 ppm, 40–55 ppm and 55–95 ppm, respectively [47,49–52].

The methyl compounds were divided into aliphatic methyl (bound on top of the aliphatic chains) and aromatic methyl (bound on the aromatic rings). The proportion of methyl (the sum of two kinds) decreased, from 14.99% to 1.55%, with an increase in maturity. It is worth noting that above 430 °C (Easy%Ro = 1.66), methyl became the largest group in aliphatic carbon, indicating that—above this temperature point—the samples only had generation potential for short-chain hydrocarbons.

Methylene accounted for the largest proportion (23.22%) of aliphatic carbon in the original kerogen. With increasing maturity, the methylene content declined to 0.71%, and the relative proportion declined from 23.92% to 4.67% within the temperature range 350–400 °C (Easy%Ro = 0.80–1.26), representing the Easy%Ro range for late oil generation. Thereafter, the methylene proportion decreased from 4.67% to 0.17% until the end of the 'gas window'.

The proportion of methine declined from 15.40% to 0.63% between 350 °C and 380 °C (Easy%Ro = 0.80–1.04). Like methine, quaternary aliphatics also decreased, from 7.25% to 0.64%, across the entire temperature range, and particularly rapidly between 350 °C and 370 °C (Easy%Ro = 0.80–0.94). This indicates that in the oil window, almost all of the aliphatic chains broke from the kerogen structure to generate oil or gas, and the ratio of aliphatic carbon decreased sharply in the oil window (Fig. 4). Sudden variations in the chemical structure of kerogen have also been previously reported [17,39]. After the oil window, the proportion of total aliphatic carbon changed at a lower rate (Fig. 4).

3.4.3. Aromatic carbon

The fraction of aromatic carbon is displayed in Table 3 and Fig. 4.

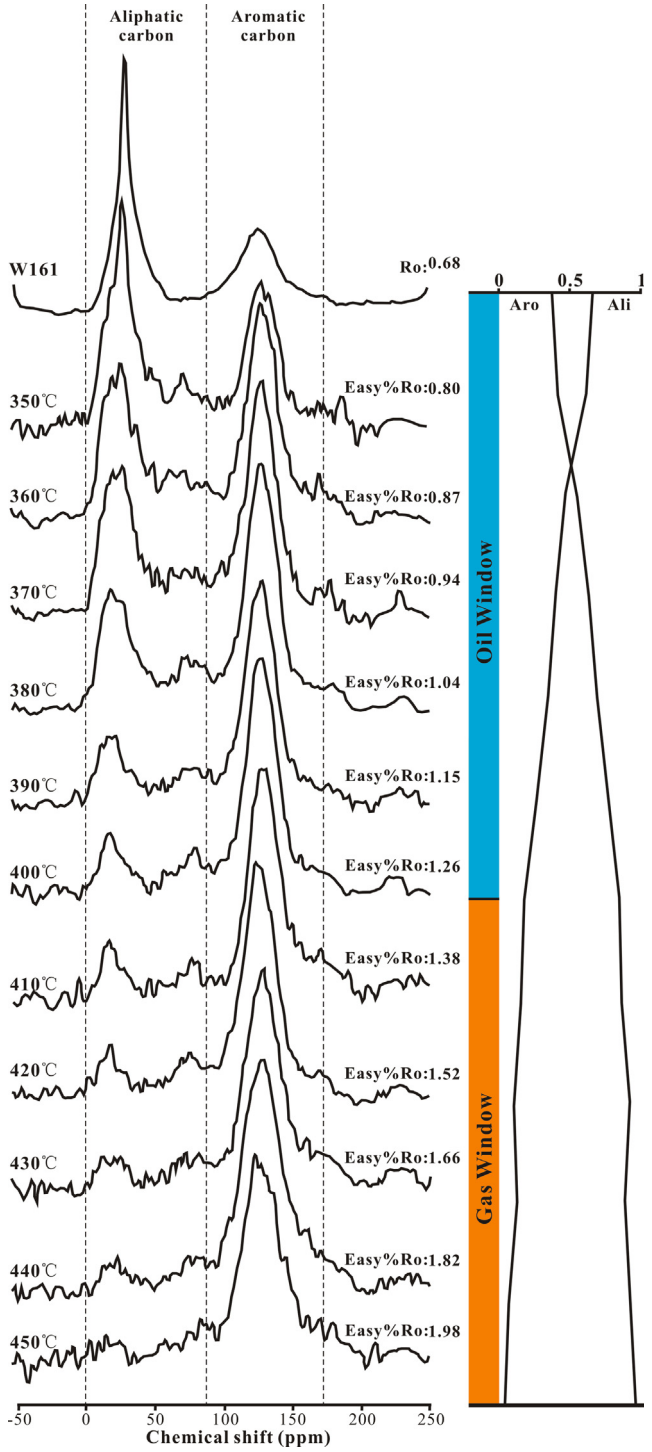

Fig. 3. Solid-state ^{13}C NMR spectra of kerogen and its residues.

The aromatic carbon proportion increased from 36.57% to 93.47% during the pyrolysis process, which was opposite to that of aliphatics; aromatic carbon increased rapidly between 350 °C and 400 °C (Easy% Ro = 0.80–1.26). The aromatic carbon was divided into four main components: (1) protonated (f_a^H), (2) bridgehead (f_a^B), (3) branched (f_a^S) and (4) oxy-aromatic (f_a^O), and the chemical shifts of these components were 95–118 ppm, 118–135 ppm, 135–145 ppm and 145–155 ppm, respectively [27,49–52]. The proportions of these four aromatic components increased with maturity due to the decrease in the proportion of aliphatic carbon, and the condensation of aromatic clusters occurred near the oil peak.

Among the aromatic carbon species, protonated aromatic carbon (f_a^H) was not attached to any other group; branched aromatic carbon (f_a^S) was attached to the aliphatic chains or methyl; and oxy-aromatic carbon (f_a^O) was attached to the oxygen atoms. These three types of aromatic carbon species were different from the bridgehead aromatic carbon, which was connected to the aromatic rings. Thus, these four types of aromatic carbon could be divided into two families, namely edge aromatic carbon (i.e. protonated, branched, and oxy-aromatic carbon) and bridgehead aromatic carbon. The proportion of bridgehead aromatic carbon increased from 9.67% to 38.79% below 420 °C (Easy% Ro = 1.52) and then increased at a lower rate. To reflect the condensation degree of the aromatic group, the X_{BP} (the ratio of bridgehead aromatic carbon to edge aromatic carbon) was calculated (Table 3), which indicates the condensation and evolution stage of kerogen [53]. In this case, X_{BP} changed from 0.36 at the initial kerogen stage to 0.71 at 450 °C (Easy%Ro = 1.98). This means that with increasing maturity, the degree of condensation was improved as well. It is worth noting that X_{BP} remained stable at approximately 0.7 within the temperature range of 420–450 °C (Easy%Ro = 1.52–1.98); however, the proportion of aromatic carbon gradually increased within the same temperature range (Table 3, Fig. 4). Thus, after the oil window, the degree of condensation did not increase with an increase in temperature. A relatively stable structure might present within this temperature range, within which the X_{BP} (the proportion of bridgehead carbon to aromatic peripheral carbon) value tended to stabilise (at 420–450 °C or above).

3.4.4. Aliphatic chains and aromatic clusters

The average aliphatic chain length (Cn') represents either the average length of aliphatic chains or half the length of aliphatic chains in two aromatic clusters [54,55]. This can be calculated from the relative amount of branched aromatic carbon and aliphatic carbon. Values of Cn' are shown in Table 3 and Fig. 5. Fig. 5 shows that Cn' decreased from 7.25 to 0.12 during the entire process, whereby it rapidly declined from 7.25 to 0.64 within the temperature range 350–400 °C (Easy%Ro = 0.80–1.26) and remained < 1 thereafter. This indicates that after the oil window, there were only a few aliphatic carbons attached to the kerogen structure and the oil generation potential was much reduced.

To study the size of the aromatic clusters, χ_{edge} was calculated as the proportion of edge carbon to aromatic carbon, which was used to calculate nC_{min} as in previous studies [15,56]. As shown in Table 3, χ_{edge} decreased from 0.95 to 0.31 across the entire temperature range. This indicates that with an increase in temperature, the proportion of edge carbon declined, while the proportion of the bridgehead aromatic carbon increased (Fig. 6a). nC_{min} was further used to estimate the number of carbon atoms in the aromatic clusters and it can also be used to estimate the average aromatic cluster size [15,56]. During pyrolysis, nC_{min} increased from 6.70 to 62.58 (Fig. 6b). This increase indicated that the average size of the aromatic clusters increased with an increase in Ro.

The χ_{edge} and nC_{min} parameters indicate that the aromatic clusters became larger and the degree of condensation increased. Both χ_{edge} and nC_{min} showed an apparent change from 350 °C to 400 °C (Easy% Ro = 0.80–1.26). Further change was not detected beyond this range.

Values of X_{BP} were obtained for three types of kerogen from previously published research (Table 4). The average X_{BP} values of type I, II and III kerogen were 0.27, 0.36 and 0.56, respectively. The average basic aromatic units were inferred as follows: type I kerogen has one or two aromatic ring clusters; the average basic aromatic unit of type II kerogen has two to three aromatic ring clusters; and average aromatic unit of type III kerogen is a tetracyclic aromatic cluster with primary catenation [56]. Descriptive statistics for X_{BP} are shown in Table 4 and Fig. 7. The characteristics of the basic aromatic units of the three types of kerogens were different, indicating that the starting points of the thermal evolution of the three kerogen types were different. In this study, 0.27 was used as the initial X_{BP} value for the evolution Type I

Table 3
NMR parameters.

Sample (Easy% Ro)	Aliphatic (%, 5–95 ppm)						Aromatic (%, 95–150 ppm)				f_{al}%	f_{ar}%	X_{BP}[a]	Cn'[b]	χ_{edge}[c]	nC_{min}[d]	I_{ar}[e]
	f_{CH3al}	f_{CH3ar}	f_{CH2}	f_{CH}	f_C	f_O	f_a^H	f_a^B	f_a^S	f_a^O							
W161 (0.68)	4.38	10.61	23.22	15.40	7.25	2.56	15.65	9.67	7.29	3.96	63.43	36.57	0.36	7.25	0.95	6.70	–
350 °C (0.80)	5.94	8.95	23.92	11.12	5.14	4.22	17.53	11.03	8.55	3.62	59.28	40.72	0.37	5.89	0.88	7.66	0.01
360 °C (0.87)	2.46	5.20	18.63	10.59	5.21	4.07	20.82	15.21	13.02	4.79	46.17	53.83	0.39	3.15	0.62	15.71	0.02
370 °C (0.94)	2.81	7.07	14.12	7.55	3.65	2.88	25.04	18.38	13.18	5.33	38.08	61.92	0.42	2.35	0.65	14.21	0.03
380 °C (1.04)	2.10	5.84	14.42	3.59	3.86	3.75	24.49	21.30	16.29	4.36	33.57	66.43	0.47	1.70	0.55	19.57	0.05
390 °C (1.15)	1.59	3.46	9.21	3.02	3.64	4.64	25.10	25.01	18.42	5.91	25.55	74.45	0.51	1.20	0.48	25.58	0.03
400 °C (1.26)	1.02	1.98	4.67	2.99	2.53	4.09	23.12	32.01	23.98	3.61	17.28	82.72	0.63	0.64	0.36	46.45	0.13
410 °C (1.38)	1.03	2.19	4.47	3.12	1.92	3.17	21.19	32.70	21.28	6.97	15.91	84.09	0.66	0.64	0.37	43.06	0.03
420 °C (1.52)	0.93	1.32	4.22	1.17	1.35	1.66	24.23	36.73	24.45	3.94	10.65	89.35	0.70	0.38	0.34	51.77	0.04
430 °C (1.66)	0.46	5.35	2.36	1.40	1.69	2.37	21.95	35.37	20.75	6.50	13.63	86.37	0.72	0.40	0.40	38.11	0.02
440 °C (1.82)	0.74	1.99	2.05	1.03	0.38	1.51	19.87	37.33	24.47	8.08	7.69	89.76	0.71	0.23	0.34	51.37	−0.01
450 °C (1.98)	0.58	0.98	0.71	0.63	0.64	0.80	20.49	38.79	27.30	6.90	4.33	93.47	0.71	0.12	0.31	62.58	0.00

[a] Ratio of bridgehead carbon to aromatic peripheral carbon.
[b] Ratio of branched carbon to aliphatic carbon.
[c] $\chi_{edge} = (f_a^H + f_a^O)/f_{ar} + \chi_{CH3ali} + \chi_{CH3aro} + \chi_{C=O}$.
[d] $nC_{min} = 6/\chi^2_{edge}$.
[e] Iar = X_{BP} (i) – X_{BP} (i-1) (i = 1…n).

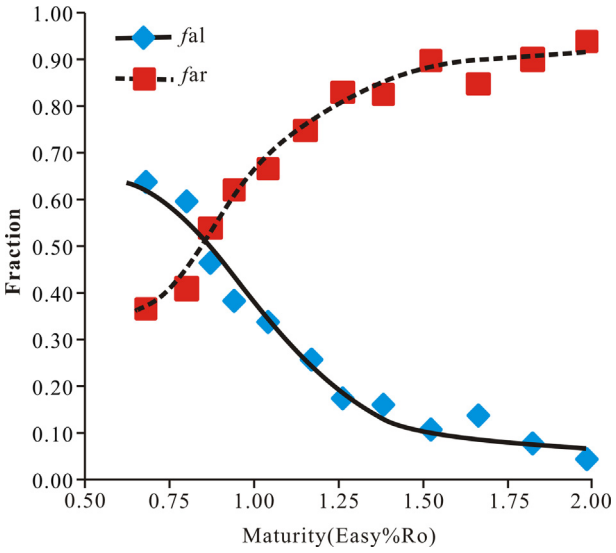

Fig. 4. Proportion of aliphatic and aromatic carbon.

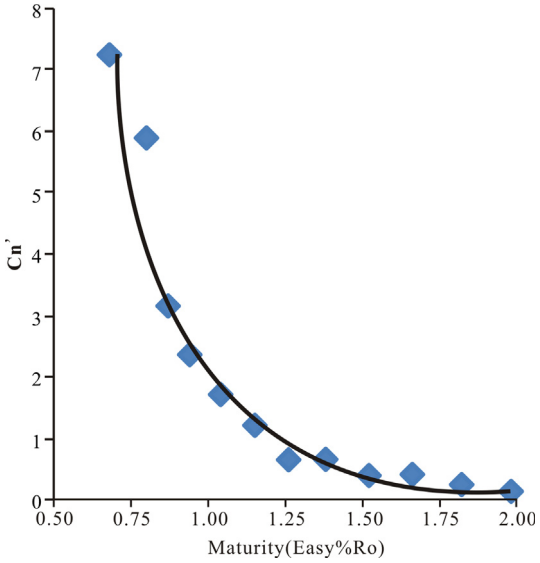

Fig. 5. Changes in the average aliphatic chain length (Cn') with temperature.

kerogen, i.e. X_{BP} (0).

To describe the change in the aromatic clusters, the average aromatic cluster increment (I_{ar}) is proposed, which can be calculated using X_{BP} in Eq. (2):

$$Iar = X_{BP}(i) - X_{BP}(i-1),\ (I=1...n) \quad (2)$$

where X_{BP} (i) denotes X_{BP} values at different temperature points; X_{BP} (0) is the average X_{BP} of Type I kerogen; and X_{BP} (1) is the initial kerogen in this study. I_{ar} denotes the aromatic unit growth between two adjacent temperature points, values of which are listed in Table 3.

Changes in I_{ar} values were not dramatic, and there was no change between maturity values of 1.66 to 1.98. This indicates that the kerogen structure was similar within this maturity range. ΣI_{ar} was calculated to assess the growth of the aromatic units during the Type I kerogen heating process. The average X_{BP} of Type I kerogen was included in this index to show which kind of aromatic unit condensed in the molecular structure. Therefore, the first point of ΣI_{ar} is the X_{BP} of Type I kerogen, and the ΣI_{ar} curve is the thermal evolution curve for Type I kerogen (Fig. 7). This increased from 0.27 to 0.72, and there was a rapid increase from 370 °C to 410 °C (Easy%Ro = 0.94–1.38) due to the separation of the small-sized aromatic clusters. Within the 'gas window', ΣI_{ar} was approximately 0.70 as the condensation reaction led to the larger-sized aromatic clusters re-combining with the residues, leading to the increase in I_{ar} in the next temperature range. In the 'gas window', the size of recombined aromatic clusters remained stable and did not tend to increase, indicating that ΣI_{ar} was approximately 0.70.

Possible aromatic units that increased during the pyrolysis process can be divided into three groups, as shown in Fig. 7. The 'Stage' A represents changes in the aromatic units during the early stages of oil generation. One-to-three-ring aromatic hydrocarbons might appear in the average kerogen molecular structure. While the aliphatic chain broke during this process, the aromatic cluster showed no change. 'Stage' B represents the rapid increase of the kerogen molecular structure size. During the maturity range 0.87–1.26, the average size of the aromatic clusters increased to a four-to-five-ring structure. 'Stage' C represents a stable phase. During this process, the primary catenation aromatic clusters could not satisfy the increased X_{BP} needs of the sample, and a circular catenation aromatic cluster was formed. Six-to-seven-ring aromatic structures appeared during this maturity range, indicating that the condensation degree of kerogen was high and that aromatic clusters with more than seven rings might be present in the kerogen.

ΣI_{ar} was used to estimate the average aromatic cluster increment and to assess the size of clusters that re-combined to the residues during

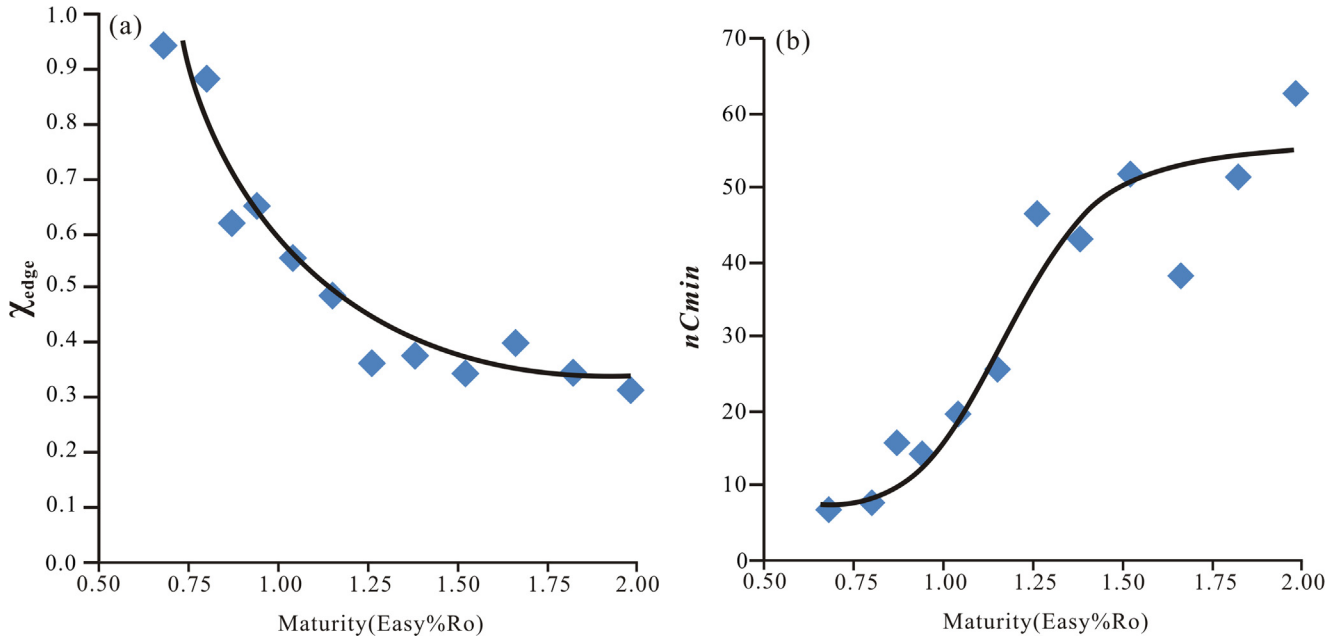

Fig. 6. Variations in the edge carbon ratio and nC_{min}.

condensation. This means that the single aromatic ring structure represented by ΣI_{ar} was the average size of the aromatic cluster that combined with the residues.

As an effective tool, ΣI_{ar} could help determine the typical kerogen molecular structure during thermal evolution. In Fig. 7, the curve indicates changes in ΣI_{ar} as maturity increases, and the three boxes might represent the aromatic cluster size as previously mentioned. Based on the curve, aromatic clusters appear to the average kerogen molecular and these three boxes in Fig. 7 indicate which clusters combined with the structure. Fig. 7, therefore, provides a clear direction for the establishment of the structure of kerogen during its thermal evolution. It should be noted that in molecular simulations, the actual increase in the aromatic unit (i.e. the molecular structure) must be slightly larger than the calculated ΣI_{ar} aromatic unit in order accurately establish the molecular structure.

3.4.5. Condensation index

Decomposition (kerogen structure was broken under pyrolysis) and condensation (interconnection of different organic structures) reactions occurred throughout the entire temperature range. Decomposition reactions dominated the lower temperatures while condensation dominated the period after the oil peak maturity. To evaluate the degree of condensation, a condensation index was developed. As Eq. (3) and Eq. (4) show, the condensation index was composed of two parts:

$$Con_L = (f^S{}_a - f_{CH3al} - f_{CH3ar})/(f^H{}_a + f^B{}_a + f^O{}_a) \quad (3)$$

$$Con_U = f^S{}_a/(f^H{}_a + f^B{}_a + f^O{}_a) \quad (4)$$

Branched aromatic carbon is the most significant functional group during condensation reactions. Therefore, the ratio of branched carbon to other aromatic carbon is used to calculate the condensation index. In Eq. (3), the lower limit (Con_L) represents the lowest condensation degree of differently matured kerogen. In the calculations, methyl is used

Table 4
Kerogen type and statistic X_{BP} values.

Type I kerogen	X_{BP}	Reference	Type II kerogen	X_{BP}	Reference	Type III kerogen	X_{BP}	Reference
Morocco	0.28	Zhao et al. [52]	Huadian	0.48	Zhao et al. [52]	Gippsland	0.61	Kelemen et al. [45]
Huadian	0.25	Guan et al. [55]	Longkou	0.24		Proprietary	0.45	
Huadian	0.20	Tong et al. [46]	Tongchuan	0.35		Douala	0.40	Behar et al. [59]
Green River	0.40	Kelemen et al. [45]	Yilan	0.49		KQ-4456	0.42	Wei et al. [50]
Rundle	0.19		Toarcian shale	0.40	Behar et al. [59]	KQ-4463	0.52	
Green river	0.23	Behar et al. [59]	Zhuanhua	0.38	Huang et al., 2018	KQ-4949	0.57	
Maoming	0.36	Gao et al. [39]	Burma	0.31	Behar et al. [59]	KQ-4467	0.58	
			Duvernay	0.28	Kelemen et al. [45]	AR-2719	0.62	
			Oxford Clay	0.37		KQ-2718	0.63	
			Paradox	0.41		KQ-2717	0.60	
			Malm	0.30		AR-2720	0.65	
			Draupne	0.38		KP-85	0.65	
			Bakken	0.32		AR-2721	0.64	
			Monterey	0.30				
Average	0.27			0.36			0.56	
Min	0.19			0.24			0.40	
Q1	0.22			0.30			0.52	
Q2	0.24			0.36			0.60	
Q3	0.36			0.40			0.63	
Max	0.40			0.49			0.65	

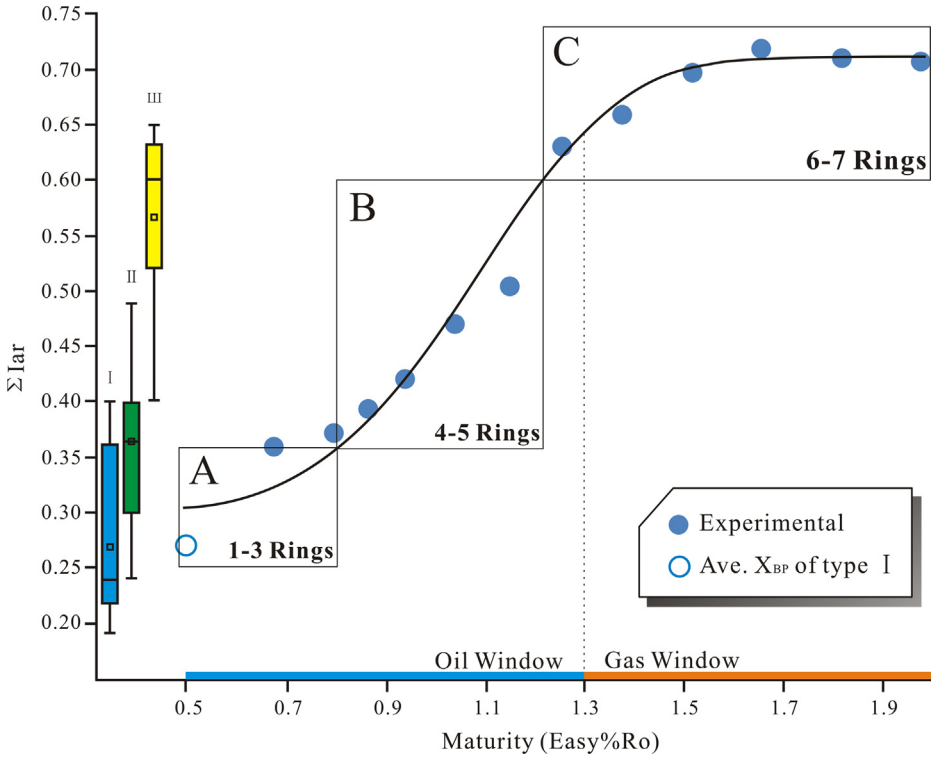

Fig. 7. Changes in the aromatic clusters of Type I kerogen during its thermal evolution: a tool for determining the structure of kerogen.

to limit the branched carbon since aliphatic chains and methyl are attached to the aromatic clusters through the branched carbon. However, as some aliphatic chains are also attached to other aliphatic chains, Con_L could be negative. In Eq. (4), the upper limit (Con_U) represents the highest degree of condensation for kerogen. In this calculation, all of the branched aromatic carbons are thought to connect different aromatic clusters. Therefore, the degree of condensation lies between Con_L and Con_U.

The results of Con_L and Con_U are shown in Fig. 8. During the kerogen maturation process, the values of Con_L increased from –0.26 to 0.39 and Con_U values increased from 0.25 to 0.41. These parameters further used to estimate the degree of condensation directly. The values

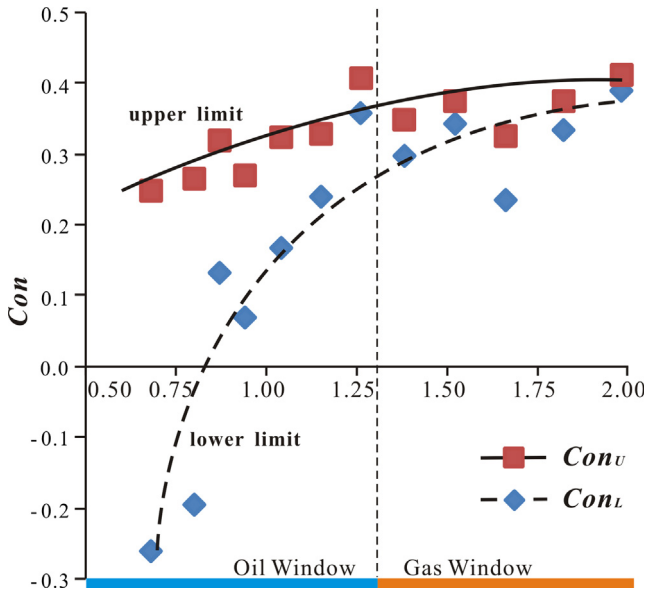

Fig. 8. *Con* index (condensation degree) change with respect to maturity.

of Con_L were positive around the oil peak maturity (Fig. 8). With increasing maturity, the difference between Con_L and Con_U was gradually reduced. This indicates that the index becomes more precise as maturity increases. However, the points and curves in Fig. 8 do not accurately reflect the degree of condensation, although these data could be used as limiting values, whereby the degree of condensation for different degrees of maturity lies between these two curves (Fig. 8).

3.5. Molecular structure model for kerogen and its structural changes

Typical molecular structure models were established for kerogen using ACD (molecular simulation software) [57] and gNMR 5.0.6 (Ivorysoft) [58] software; ACD was used to develop the models and gNMR was used to calculate and simulate the ^{13}C NMR spectra of models. The test ^{13}C NMR spectra and simulated ^{13}C NMR spectra were also compared. The model parameters were varied to correct the simulated spectra until a high similarity was achieved (i.e. to obtain similar major peak positions, widths and heights). This process is explained in detailed elsewhere [17,39].

Six models were developed. The molecular structures and the spectra for each are shown in Fig. 9, which includes the changes in the aliphatic carbon and aromatic clusters. As temperature increased, the aliphatic chains were rapidly cracked from the structure. The number and size of aromatic clusters also increased simultaneously. The spectra of the structures indicate that the simulation spectra were similar to the test spectra, meaning that the structural models well represent the average molecular model of the residues. The characteristics of the structures are also shown in Fig. 9, which were used to verify the correctness of the structural models. The values of X_{BP} for the simulated structures were close to those of the tests, which indicated the accuracy of the molecular models.

The structures indicate that the kerogen samples had a large hydrocarbon-generation potential below 390 °C, and there were few aliphatic chains or small-sized aromatic clusters in the models above this temperature point. This indicates that the majority of the soluble hydrocarbons are generated below this temperature. Above 390 °C, the

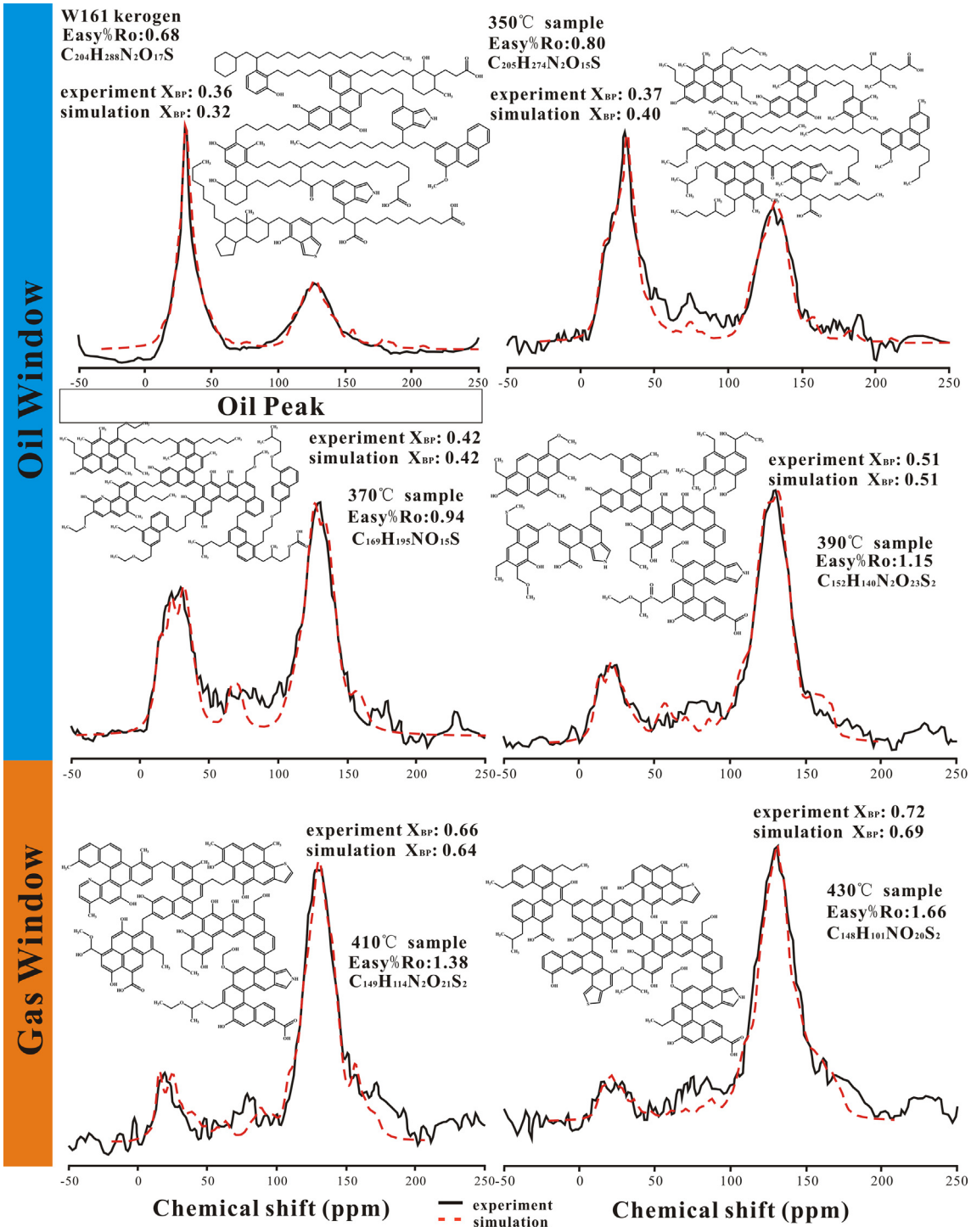

Fig. 9. Six chemical structures and their associated spectra.

models of the residues were mainly formed of aromatic carbon. The chemical structures showed that during pyrolysis, the aliphatic chains and small-sized aromatic clusters separated from the kerogen structure to generate oil, and the kerogen evolved into a macromolecular-fused ring under high temperatures.

As shown in Fig. 9, kerogen structures varied significantly between the 'oil window' and the 'gas window'. As previously mentioned, both the length of the aliphatic chains and the size of the aromatic clusters have changed between these two maturity ranges. Furthermore, the relative proportions of aliphatic and aromatic compounds, X_{BP}, and Cn' showed a significant change after peak oil generation (Easy% Ro = 0.94–1.25). These phenomena indicate that there was a structural jump during the transition from the 'oil window' to the 'gas window'. This finding is consistent with our previous research [39].

4. Conclusions

An pyrolysis experiment was carried out on kerogen isolated from source rock. Variation in the chemical structure of kerogen during maturation was studied. As maturity increased, the proportion of aliphatic carbon declined whereas aromatic carbon increased. Aliphatic chains and small-sized aromatic clusters were present during the

majority of the oil-generating process. It is noted that, after the maturity of oil peak, the condensation reaction was the dominant factor responsible for variations in the structure of kerogen. Almost all the measured parameters (i.e. the proportion of aliphatic and aromatic carbon, X_{BP} and Cn') indicated that there was a rapid structural change in the molecular structure of kerogen. Within the 'gas window', the chemical structure of kerogen was stable, with minor variations.

From our analysis, ΣI_{ar} and *Con* were calculated. ΣI_{ar} reflected the size of aromatic clusters, which increased in the generalised kerogen molecular models. This could be a useful tool to help determine the molecular structure. Additionally, *Con* (Con_L and Con_U) was able to estimate the change in condensation during the heating process. Both of these factors could be used to further study the molecular structure of kerogen. Furthermore, our six molecular models provide a more intuitive way to observe the structure of kerogen during the hydrocarbon-generating process.

Declaration of Competing Interest

The authors declare that they have no known competing financial interests or personal relationships that could have appeared to influence the work reported in this paper.

Acknowledgements

This research was supported by the Strategic Priority Research Program of the Chinese Academy of Sciences, China (XDA14010102), the State Key Laboratory of Organic Geochemistry, GIGCAS (Grant No. SKLOG-201809), and the Foundation for Innovative Research Groups of the National Natural Science Foundation of China (Grant No. 41621062). Thanks to Dr. Wu Li (China University of Mining and Technology) for guidance on molecular model construction from the NMR data. Thanks to the editors and reviewers for their valuable comments on this article.

Contributors

Tian Liang completed the experiments, acquired the data and drafted the paper. Dr. Yan-Rong Zou designed the experiments and finalized the manuscript. Dr. Zhao-Wen Zhan processed the samples. Xiao-Hui Lin and Jun Shi assisted in some experiments. Ping'an Peng provided the samples, noted the deficiency and helped to improve this paper.

References

[1] Sert M, Ballice L, Yuksel M, Saglam M. Effect of mineral matter on product yield and composition at isothermal pyrolysis of Turkish oil shales. Oil Shale 2009;4:463–74.
[2] Durand B. Sedimentary organic matter and kerogen. Definition and quantitative importance of kerogen. In: Durand, B. (Ed.), Kerogen, Insoluble Organic Matter from Sedimentary Rocks. Editions Technip, Paris, 1980; p. 13–34.
[3] Liu HP, Liang WX, Wu MH, Wang Q. Co-combustion of Oil shale retorting solid waste with cornstalk particles in a circulating fluidized bed. Energy Fuels 2015;29:6832–8.
[4] Vandenbroucke M, Largeau C. Kerogen origin, evolution and structure. Org Geochem 2007;38:719–833.
[5] Wang Q, Hou YC, Wu WZ, Liu Q, Liu ZY. The structural characteristics of kerogens in oil shale with different density grades. Fuel 2018;219:151–8.
[6] Boucher RJ, Standen G, Patience RL, Eglinton G. Molecular characterisation of Kimmeridge Clay Formation kerogen by mild selective chemical degradation and solid state 13C NMR. Org Geochem 1990;16:951–8.
[7] Mann AL, Patience RL, Poplett IJF. Determination of molecular structure of kerogens using ^{13}C NMR spectroscopy I: effects of variation in kerogen type. Geochim Cosmochim Acta 1991;55:2259–68.
[8] Patience RL, Mann AL, Poplett IJF. Determination of molecular structure of kerogens using ^{13}C NMR spectroscopy II: the effects of thermal maturation on kerogens from marine sediments. Geochim Cosmochim Acta 1992;56:2725–42.
[9] Burlingame AL, Haug PA, Schnoes HK, Simoneit BR. Fatty acids derived from the Green River Formation oil shale by extractions and oxidations – a review. In: Schenck PA, Havenaar I, editors. Advances in organic geochemistry. Oxford: Pergamon Press; 1969. p. 85–129.
[10] Carlson GA. Computer simulation of the molecular structure of bituminous coal. Energy Fuels 1992;6:771–8.
[11] Murgich J, Rodriguez J, Aray Y. Molecular recognition and molecular mechanics of micelles of some model asphaltenes and resins. Energy Fuels 1996;10:68–76.
[12] Wang Q, Pan S, Bai JR, Chi MS, Cui D, Wang ZC, et al. Experimental and dynamics simulation studies of the molecular modeling and reactivity of the Yaojie oil shale kerogen. Fuel 2018;230:319–30.
[13] Craddock PR, Le Doan TV, Bake KD, Polyakov M, Charsky AM, Pomerantz AE. Evolution of kerogen and bitumen during thermal maturation by semi-open pyrolysis investigated by infrared spectroscopy. Energy Fuels 2015;29:2197–210.
[14] Craddock PR, Bake KD, Pomerantz AE. Chemical, molecular, and microstructural evolution of kerogen during thermal maturation: Case study from the Woodford Shale, Oklahoma. Energy Fuels 2018;32:4859–72.
[15] Mao JD, Fang XW, Lan YQ, Schimmelmann A, Mastalerz M, Xu L. Chemical and nanometer-scale structure of kerogen and its change during thermal maturation investigated by advanced solid-state ^{13}C NMR spectroscopy. Geochim Cosmochim Acta 2010;74:2110–27.
[16] Tong JH, Jiang XM, Han XX, Wang XY. Evaluation of the macromolecular structure of Huadian oil shale kerogen using molecular modeling. Fuel 2016;181:330–9.
[17] Huang ZK, Liang T, Zhan ZW, Zou YZ, Li MW, Peng P. Chemical structure evolution of kerogen during oil generation. Mar Pet Geol 2018;98:422–36.
[18] Zhang L, LeBoeuf J. A molecular dynamics study of natural organic matter: 1. Lignin, kerogen and soot. Org Geochem 2009;40:1132–42.
[19] Vandenbroucke M. Kerogen: from types to models of chemical structure. Oil Gas Sci Technol 2003;58:243–69.
[20] Pan CC, Jiang LL, Liu JZ, Zhang SC, Zhu GY. The effects of calcite and montmorillonite on oil cracking in confined pyrolysis experiments. Org Geochem 2010;41:611–26.
[21] Wang Q, Zou HY, Hao F, Zhu YM, Zhou XH, Wang YB, et al. Modeling hydrocarbon generation from the Paleogene source rocks in Liaodong Bay, Bohai Sea: A study on gas potential of oil-Prone source rocks. Org Geochem 2014;76:204–19.
[22] Ma Anlai. Kinetics of oil-cracking for different types of marine oils from Tahe Oilfield, Tarim Basin, NW China. J Nat Gas Geosci 2016;1:35–43.
[23] Dennis LW, Maciel GE. ^{13}C nuclear magnetic resonance studies of kerogen from Cretaceous black shales thermally altered by basaltic intrusions and laboratory simulations. Geochim Cosmochim Acta 1982;46:901–7.
[24] Witte EG, Schenk PJ, Schwoshau K. Structural modifications of kerogen during natural evolution as derived from ^{13}C CP/MAS NMR, IR spectroscopy and Rock-Eval pyrolysis of Toarcian shales. Org Geochem 1988;13:1039–44.
[25] Solum MS, Sarofim AF, Pugmire RJ, Fletcher TH, Zhang HF. ^{13}C NMR analysis of soot produced from model compounds and a coal. Energy Fuels 2001;15:961–71.
[26] Wang ZC, Wang Q, Jia CX. Structural changes in oil sand bitumen during pyrolysis. J Therm Anal Calorim 2016;127:2215–23.
[27] Lille Ü, Heinmaa I, Pehk T. Molecular model of Estonian kukersite kerogen evaluated by ^{13}C MAS NMR spectra. Fuel 2003;82:799–804.
[28] Li ZK, Wei XY, Yan HL, Zong ZM. Insight into the structural features of Zhaotong lignite using multiple techniques. Fuel 2015;153:176–82.
[29] Siskin M, Scouten CG, Rose KD, Aczel T, Colgrove SG, Pabst Jr RE. Detailed structural characterization of the organic material in rundle Ramsay crossing and Green River oil shales. In: Snape C, editor. Composition, geochemistry and conversion of oil shales. Dordrecht: Kluwer Academic Publishers; 1995. p. 143–58.
[30] Given PH, Spackman W, Painter PC, Rhoads CA, Ryan NJ. The fate of cellulose and lignin in peats: an exploratory study of the input to coalification. Org Geochem 1984;6:399–407.
[31] Kelemen SR, Afeworki M, Gorbaty ML. Characterization of organically bound oxygen forms in Lignites, Peats, and Pyrolyzed Peats by X-ray photoelectron spectroscopy (XPS) and Solid-State ^{13}C NMR methods. Energy Fuels 2002;16:1450–62.
[32] Kelemen SR, Georgy GN, Gorbaty ML. Direct determination and quantification of sulphur forms in heavy petroleum and coals 1. The X-ray photoelectron spectroscopy (XPS) approach. Fuel 1990;69:939–44.
[33] Pietrzak R, Wachowska H. The influence of oxidation with HNO3 on the surface composition of high-sulphur coals: XPS study. Fuel Process Technol 2006;87:1021–9.
[34] Li J, Zhou SX, Gaus G, Li YJ, Ma Y, Chen KF, et al. Characterization of methane adsorption on shale and isolated kerogen from the Sichuan Basin under pressure up to 60 MPa: Experimental results and geological implications. Int J Coal Geol 2018;189:83–93.
[35] Huang L, Ning ZF, Wang Q, Qi RR, Zeng Y, Qin HB. Molecular simulation of adsorption behaviors of methane, carbon dioxide and their mixtures on kerogen: Effect of kerogen maturity and moisture content. Fuel 2018;211:159–72.
[36] Durand B, Nicaise G. Procedures of kerogen isolation. In: Durand, B. (Ed.), Kerogen, Insoluble Organic Matter from Sedimentary Rocks. Editions Technip, 1980; p. 35–53.
[37] General Administration of Quality Supervision, Inspection and Quarantine of the People's Republic of China, Standardization Administration of the People's Republic of China. Isolation method for kerogen from sedimentary rock. GB/T 19144-2010.
[38] Sweeney JJ, Burnham AK. Evaluation of a simple model of vitrinite reflectance based on chemical kinetics. Am Assoc Pet Geol Bull 1990;74:1559–70.
[39] Gao Y, Zou YR, Liang T, Peng P. Jump in the structure of Type I kerogen revealed from pyrolysis and ^{13}C DP MAS NMR. Org Geochem 2017;112:105–18.
[40] Liu HM, Mei GL, Xu Z, Liu P, Li Y. Quantitative analysis of Fe and Co in Co-substituted magnetite using XPS: The application of non-linear least squares fitting (NLLSF). Appl Surf Sci 2016;389:438–46.
[41] Jarvie DM, Claxton BL, Henk F, Breyer JT. Oil and shale gas from the Barnett Shale, Fort Worth Basin, Texas. Am Assoc Pet Geol 2001;10:A100.
[42] Qin KZ, Wu XL. An approach to estimate the average structural unit weight of

kerogen. Org Geochem 1990;16:995–1000.
[43] Liao YH, Zheng YJ, Pan CC, Sun YG, Geng AS. A method to quantify C1–C5 hydrocarbon gases by kerogen primary cracking using pyrolysis gas chromatography. Org Geochem 2015;79:49–55.
[44] Siskin M, Brons Jr GJFP. Disruption of kerogen-mineral interactions in oil shales. Energy Fuels 1989;32:248–52.
[45] Kelemen SR, Afeworki M, Gorbaty ML, Sansone M, Kwiatek PJ, Walters CC, et al. Direct characterization of kerogen by X-ray and Solid-State ^{13}C nuclear magnetic resonance methods. Energy Fuels 2007;21:1548–61.
[46] Tong JH, Han XX, Wang S, Jiang XM. Evaluation of structural characteristics of Huadian oil shale kerogen using direct techniques (Solid-State ^{13}C NMR, XPS, FT-IR, and XRD). Energy Fuels 2011;25:4006–13.
[47] Cao XY, Yang J, Mao JD. Characterization of kerogen using solid-state nuclear magnetic resonance spectroscopy: A review. Int J Coal Geol 2013;108:83–90.
[48] Martin JT, Lain JFP, Alan G. Structure of Green River oil shale kerogen determination using solid state ^{13}C NMR spectroscopy. Fuel 1986;65:541–6.
[49] Meng LZ. Organic spectral analysis. Wuhan: Wuhan University Press; 2003.
[50] Wei ZB, Gao XX, Zhang DJ, Da J. Assessment of thermal evolution of kerogen geopolymers with their structural parameters measured by solid-state ^{13}C NMR spectroscopy. Energy Fuels 2005;19:240–50.
[51] Wang Q, Hou YC, Wu WZ, Yu Z, Ren SH, Liu QY, et al. A study on the structure of Yilan oil shale kerogen based on its alkali-oxygen oxidation yields of benzene carboxylic acids, ^{13}C NMR and XPS. Fuel Process Technol 2017;166:30–40.
[52] Zhao XS, Liu ZY, Lu ZH, Shi L, Liu QY. A study on average molecular structure of eight oil shale organic matters and radical information during pyrolysis. Fuel 2018;219:399–405.
[53] Clough A, Sigle JL, Jacobi D, Sheremata J, White JL. Characterization of kerogen and source rock maturation using solid-state NMR spectroscopy. Energy Fuels 2015;29:6370–82.
[54] Fletcher TH, Gillis R, Adams J, Hall T. Characterization of macromolecular structure elements from a Green River oil shale, II. Characterization of pyrolysis products by ^{13}C NMR, GC/MS, and FTIR. Energy Fuels 2014;28:2959–70.
[55] Guan XH, Liu Y, Wang D, Wang Q, Chi MS, Liu S, et al. Three-dimensional structure of a Huadian oil shale kerogen model: An experimental and theoretical study. Energy Fuels 2015;29:4122–36.
[56] Solum MS, Pugmire RJ, Grant DM. ^{13}C solid-state NMR of argonne premium coals. Energy Fuels 1989;3:187–93.
[57] ACD/Labs, 2016. < http://www.acdlabs.com/resources/freeware/chemsketch/ > .
[58] gNMR, Version 5.0.6-DEMO by Cherwell Scientific Publishing. http://www.cherwell.com.
[59] Behar F, Vandenbroucke M. Chemical modelling of kerogens. Org Geochem 1987;1:15–24.